PAPER • OPEN ACCESS

Density profiles in stellarators: an overview of particle transport, fuelling and profile shaping studies at TJ-II

To cite this article: J.A. Alonso *et al* 2024 *Nucl. Fusion* **64** 112018

View the article online for updates and enhancements.

Density profiles in stellarators: an overview of particle transport, fuelling and profile shaping studies at TJ-II

J.A. Alonso[1,*], D. Alegre[1], J. Alonso[1], R. Antón[1], A. Arias-Camisón[2], E. Ascasíbar[1],
A. Baciero[1], J.M. Barcala[3], M. Barnes[4], E. Blanco[1], L. Bueno[1], A. Bustos[1], S. Cabrera[1],
E. de la Cal[1], I. Calvo[1], A. Cappa[1], D. Carralero[1], R. Carrasco[1], B. Carreras[5],
R. Castro[1], A. de Castro[1], L. Cebrián[1], M. Chamorro[1], A.A. Chmyga[6], P. Colino[1], J. Duque[1],
F.J. Escoto[1], T. Estrada[1], A. Fernández[1], J. Fraguas[1], J.M. Fontdecaba[1], A. Gabriel[1],
L. García[5], I. García-Cortés[1], R. García-Gómez[1], J.M. García-Regaña[1], G. Godino-Sedano[1],
J. Gómez-Manchón[1], A. González[1], A. González-Jerez[1], V. Guisse[1],
J. Hernández-Sánchez[1], J. Hernanz[1], C. Hidalgo[1], P. Ivanova[7], A. Jiménez-Denche[1],
D. Jiménez-Rey[1], G. Kocsis[8], M. Koepke[9], A.S. Kozachek[6], F. Lapayese[1], M. Liniers[1],
D. López[1], D. López-Bruna[1], B. López-Miranda[1], E. de la Luna[1], E. Maragkoudakis[1],
F. Martín-Díaz[1], G. Martín-Gómez[1], J. Martínez-Fernández[1], K.J. McCarthy[1], F. Medina[1],
D. Medina-Roque[1], M. Medrano[1], P. Méndez[1], F.J. Miguel[1], B. van Milligen[1], A. Molinero[3],
G. Motojima[10], S. Mulas[1], M. Navarro[1], I. Nedzelskiy[11], R. Nuñez[1], M. Ochando[1],
E. Oyarzábal[1], J.L. de Pablos[1], F. Palomares[1], N. Panadero[1], F.I. Parra[12], C. Pastor[1],
I. Pastor[1], A. de la Peña[1], R. Peralta[1], A. Pereira[1], P. Pons-Villalonga[1], A.B. Portas[1],
E. Poveda[1], F.J. Ramos[1], G.A. Rattá[1], M. Redondo[1], C. Reynoso[1], E. Rincón[1],
J. de la Riva[1], C. Rodríguez-Fernández[1], A. Ros[1], E. Sánchez[1], J. Sánchez[1],
E. Sánchez-Sarabia[1], J.A. Sebastián[1], E.R. Solano[1], A. Soleto[1], T. Szepesi[8], F.L. Tabarés[1],
D. Tafalla[1], H. Takahashi[10], N. Tamura[10], H. Thienpondt[1], A. Tolkachev[1], V. Tribaldos[5],
R. Unamuno[1], J. Varela[5], J. Vega[1], J.L. Velasco[1] and I. Voldiner[1]

[1] Laboratorio Nacional de Fusión, CIEMAT, Madrid, Spain
[2] Salamanca University, Salamanca, Spain
[3] Technology Department, CIEMAT, Madrid, Spain
[4] Rudolf Peierls Centre, University of Oxford, Oxford, United Kingdom of Great Britain and Northern Ireland
[5] Universidad Carlos III, Madrid, Spain
[6] Institute of Plasma Physics of the National Science Center 'Kharkiv Institute of Physics and Technology', Kharkiv, Ukraine
[7] Bulgarian Academy of Sciences, Sofia, Bulgaria
[8] Centre for Energy Research, Budapest, Hungary
[9] Physics and Astronomy Department, West Virginia University, WV, United States of America
[10] National Institute for Fusion Science, Toki, Japan
[11] IPFN, Instituto Superior Técnico, University Lisboa, Lisboa, Portugal
[12] Princeton Plasma Physics Laboratory, Princeton, NJ, United States of America

* Author to whom any correspondence should be addressed.

CrossMark

Abstract

We provide an overview of activities carried out at the TJ-II stellarator for improving our
understanding of- and developing plasma physics models for particle density profiles in
stellarators. Namely, we report on recent progress in turbulent particle transport simulation,
validation of pellet deposition models, density profile shaping for performance control and new
experimental techniques for edge turbulence and plasma-neutral interaction.

Keywords: particle transport, fuelling, cryogenic pellet injection, stellarator

(Some figures may appear in colour only in the online journal)

1. Introduction

When devising the physics scenarios of prospective stellarator fusion power plants, the ability to predict the fusion reactants' density profiles bears an obvious importance: the number of fusion reactions per unit of volume and time is proportional to the number density of the two fusing species. Both the average density and the profile shape are important features to be able to predict. The shape of the density profile is known to substantially affect the quality of the plasma confinement [1] and the absolute electron and ion density levels determine the radiated power fraction and the proximity to the density limit, often called Sudo limit in the stellarator literature [2].

A stellarator reactor would optimally operate close to the Sudo limit to optimise power exhaust, but also would require good core confinement for economic efficiency. Both simulations and experiment indicate that the latter could benefit from some degree of profile-shaping capability. It is accepted that core fuelling by pellet injection (PI) will be required in reactor scenarios. The particle density profile will be then determined by the balance of the radially distributed particle source and the neoclassical and turbulent particle fluxes that result from the density and temperature profiles of the various plasma species. Recently, gyrokinetic simulations with realistic plasma profiles and geometry have shed some light on the turbulent particle fluxes in 3D configurations [3]. These are presented in section 2. The calculation of the pellet particle source requires the validation of ablation and plasmoid-drift physics in the complex magnetic field spectrum of stellarators. We summarise recent efforts to validate pellet particle deposition with simulations and experiments in section 3. With regard to pellet fuelling in stellarator reactors, it is interesting to note that the non-axisymmetric magnetic field structure could allow a deep core fuelling by high-speed pellets injected from the low-field side (LFS) into a favourable-drift, high-flux compression region [4].

As previously mentioned, the shape of the density profile has been shown to have a large effect on the intensity of turbulent fluctuations and the overall performance in the W7-X, TJ-II and other stellarators [4], and could affect the thermal stability properties and operational map of a stellarator reactor [5]. For the particular case of TJ-II, PIs into neutral beam-heated plasmas has allowed to obtain record confinement levels with substantially increased ion temperature. These observations are summarised in section 4. Arguably, another illustration of the effect of particle source characteristics in plasma performance is that of reduced recycling conditions. Indeed, the level of plasma recycling at the limiting surfaces or, more generally, the distribution of neutrals in the plasma edge and SOL is empirically known to affect the plasma confinement quality, which, in TJ-II, was most notorious after lithium-coating the wall [6]. This has partly motivated recent efforts to consistently model plasma and neutral dynamics in turbulent timescales [7]. Along this line, in section 5 we report on a diagnostic development at TJ-II that is capable of providing edge electron temperature and density measurements with high spatial and temporal resolution.

A notable omission in this overview is that of density limit phenomena. For both tokamaks (see e.g. [8]) and stellarators, the discussion of density limit has followed two, often confronted lines of argument, which emphasised respectively the roles of radiation power losses and transport phenomena behind confinement degradation and eventual plasma collapse. The explicit power dependence of the Sudo density limit in stellarators is in contrast with the tokamak Greenwald limit and has important implications for reactor design. Experiments at TJ-II have shown that densities attained in NBI discharges remained below the Sudo limit [9]. Lithium wall coating allowed extending the operational density range considerably, which is, at least partly, explained by the better control of plasma composition. The TJ-II diagnostic suite allows to diagnose large-scale zonal turbulent structures (zonal flows) with dual Langmuir and heavy ion beam systems. In

[10] the behaviour of zonal flows was investigated in the vicinity of the density limit. In the first Wendelstein 7-X campaigns, the range of accessible densities showed a reasonable consistency with a simple radiation and transport model in which the location of the peripheral radiation layer, caused by low-Z impurities, determines the onset of detachment and density limit [11–13]. On-going inter-machine studies, including medium and large stellarator devices, will help firming up our understanding and predictive capability of density limit in stellarators.

Although the importance of the above-mentioned observations is generally acknowledged, our understanding of the plasma physics processes that shape the density profile in stellarators (fuelling, transport, edge-core coupling, etc) is far from complete—arguably, less so than for the case of the temperature profiles [14]. Several of these physics ingredients have been investigated at the TJ-II stellarator and other devices with notable progress made in recent years in improving our fundamental understanding, documenting observations and developing experimental techniques that will allow us to test physics models and mechanisms. This manuscript is meant to provide an overview of those activities that have been conducted at TJ-II, oftentimes in connection with other stellarators such as W7-X, LHD and Heliotron J, to summarise the status of our understanding in those areas and to highlight directions of future research.

2. Turbulent particle fluxes—core particle depletion

Under general conditions with a peripheral particle source from recycling or gas puff, the particle transport predicted by neoclassical theory in stellarator plasmas has the following features: (1) it is outward-directed across the plasma radius, (2) it is too large in the core and (3) it is too small at the edge. In particular, neoclassical theory predicts strongly hollow density profiles and core particle depletion [15, 16] that, in general, are not observed in experiments [3, 16–18]. We note that moderately hollow density profiles are found in ECH heated stellarator plasmas (e.g. in TJ-II and LHD). Recently, by means of gyrokinetic simulations, it has been proven that the contribution of turbulence to the particle flux is key to explaining the experimental observations [3]. In that reference, for the first time in a W7-X plasma, the sign of the turbulent particle flux obtained from gyrokinetic simulations has been shown to agree over the entire plasma radius with the sign of the difference between the experimental and neoclassical fluxes. It is worth emphasizing that, within approximately the mid-plasma radius, the turbulent particle flux is directed inwards, compensating the outward-directed neoclassical flux. This explains why density profiles are not as hollow as neoclassical theory alone predicts. TJ-II is characterized by a large neoclassical transport which, however, results in only mild hollowness in centrally heated ECH plasmas, milder than expected on the basis of neoclassical particle fluxes (see [18]). The short mean-free-path neutral particle transport model used

in [3] is not applicable to TJ-II plasmas, so a parallel study could not yet be conducted. However, on the basis of the simulations presented here (see figure 1 and the discussion below), a similar qualitative behaviour of the gyrokinetic fluxes is to expected in TJ-II.

A key factor contributing to the turbulent particle pinch observed in simulations is the interplay of finite values in both electron and ion temperature gradients. This underscores the importance of using a realistic electron temperature gradient in gyrokinetic simulations of ion Larmor scale turbulence, which has not been a common practice in previous stellarator studies. The density gradient scan shown in figure 1 shows that this is indeed the case for both stellarators and tokamaks, and that the observation of an inward turbulent particle transport for low but positive (i.e. peaked) density gradients is a robust one. In particular, it can be observed that for a flat density profile (i.e. when the normalized density gradient $a/L_n = 0$), all the devices under consideration—W7-X, TJ-II, LHD, NCSX, the analytical tokamak known as Cyclone Base Case (CBC) and the ASDEX-Upgrade (AUG) tokamak— display inward particle fluxes when an electron temperature gradient is included in the simulations.

In preparation of an experimental verification at TJ-II, the behaviour of the gyrokinetic particle flux has been investigated in further detail, scanning the density gradient for three values of ion temperature gradient, which are chosen to be smaller than the electron temperature gradient (at TJ-II, the electron temperature value and its gradient are typically stronger than those of the ion species). Thus, as the diffusive contribution is suppressed ($a/L_n = 0$) and the ion temperature gradient vanishes, as figure 2(a) shows, the sign of the flux changes from negative to positive when turbulence is solely driven by the electron temperature gradient. Note that these results for TJ-II conditions align with those shown in figure 1, namely, an inward turbulent particle flux is found as long as the ion and electron temperature gradients take both finite values, not necessarily large or close to each other. In TJ-II already for moderate ion temperature gradients, as can be seen in figure 2(a), the turbulent particle convection becomes negative. These results indicate that TJ-II core scenarios (see e.g. [19]) with flat density and slight peaked ion temperature profile could feature an inward turbulent particle flux. Figure 2(b) shows the binormal wavenumbers most involved in the simulated particle flux and the observed phase difference between electrostatic potential and density fluctuations, which is amenable to experimental investigation. Both for the positive and negative density gradient condition, the particle transport is chiefly due to turbulent structures with spatial scales $k_y \rho_i \sim 0.5$ which, for typical TJ-II parameters, correspond to spatial scales around one centimetre. For those scales, the phase-shift between electrostatic potential and density fluctuation is predicted to be small and negative for hollow density profiles (figure 2(b) left) and about 45° for the peaked density conditions (figure 2(b) right). Finally, analytical quasi-linear arguments relate the characteristics of the underlying unstable modes and, particularly, the sign of their frequency with the
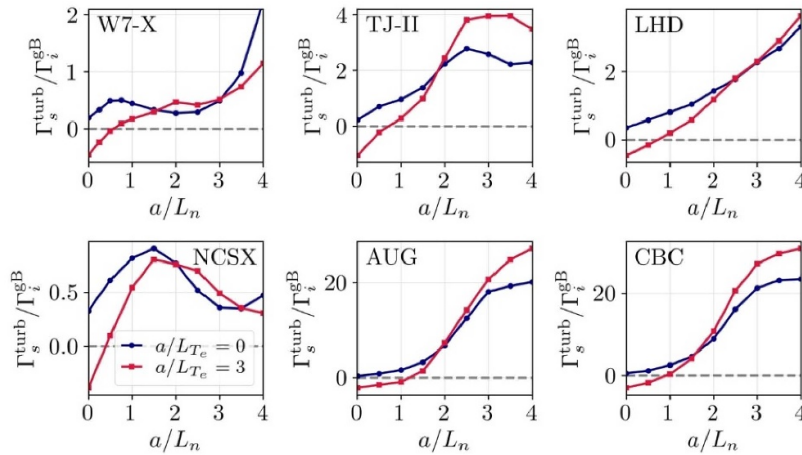
Figure 1. Turbulent particle transport in gyro-Bohm units as a function of the normalised density gradient for the W7-X, TJ-II, LHD, NCSX stellarators, and the Cyclone Base Case (CBC) and Asdex-Upgrade (AUG) tokamaks. The simulated radial position is $r/a = 0.7$. The case where the ion and electron temperature gradients are set to $a/L_{T_i} = a/L_{T_e} = 3$ is represented with red filled squares and the case with $a/L_{T_e} = 0$ and $a/L_{T_i} = 3$ is represented with blue filled circles.
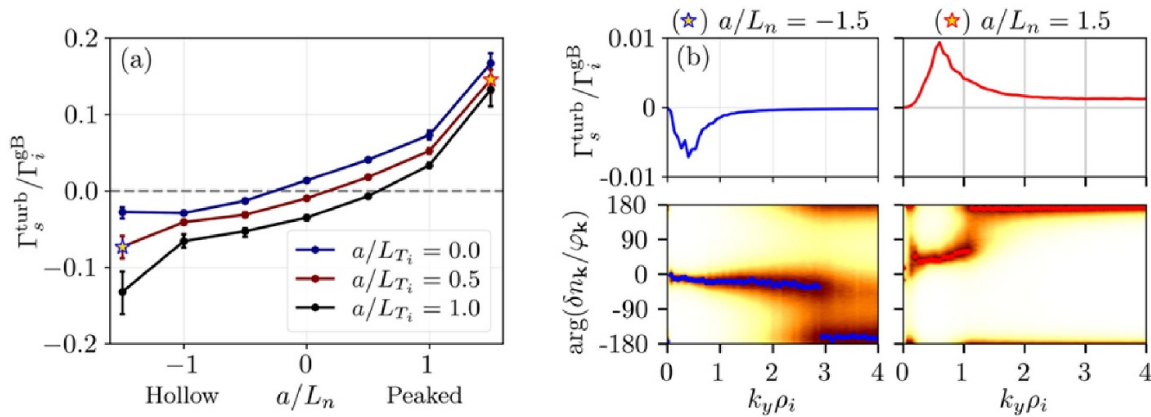

Figure 2. Turbulent particle flux obtained with electrostatic stella [12] simulations, considering kinetic ions and electrons, performed in a flux tube at $r/a = 0.6$ for the TJ-II standard configuration. The influence of the normalized density gradient is investigated for $a/L_{T_e} = 2$ and considering flat and weakly peaked ion temperature profiles (*a*). The spectrum of the turbulent particle flux and the phase-shift between the density and potential fluctuations for the two highlighted cases (blue and red stars in the left plot) are shown in (*b*).

sign of the convection and the contributions thereof (thermo-diffusion and curvature pinch or anti-pinch, see e.g. [20]). How the sign of the frequency is correlated with the sign of the fluxes in nonlinear simulations will be the matter for future numerical effort.

These numerical predictions will be the basis of dedicated experimental programs at TJ-II, in which the Heavy Ion Beam Probe provides time- and spatially-resolved measurements or proxies of electrostatic potential and electron density. Previous studies based on this diagnostic at TJ-II have shown a clear effect of the sign of the density gradient on the turbulence level [21], whereas Langmuir probe measurements illustrated the interplay between the ambient radial electric field and the cross-phase between density and poloidal electric fluctuations [22].

3. Particle source—pellet ablation/deposition in 3d magnetic fields

Cryogenic PI is currently the best candidate for efficient plasma fuelling in a fusion reactor. Although pellet ablation is generally well understood, a complete understanding of plasmoid (i.e. the ionized clouds that detach periodically from a pellet during the ablation process) homogenization remains outstanding, particularly in helical devices. Pellet particle deposition and fuelling efficiency depend strongly on the ∇B-induced drift of plasmoids, which results in an internal electrostatic potential distribution [23–25]. Such potential distribution can be modified, leading to the enhancement or reduction of the drift acceleration. The so-called internal circuit closure (ICC) arises when the plasmoid expansion along the field line
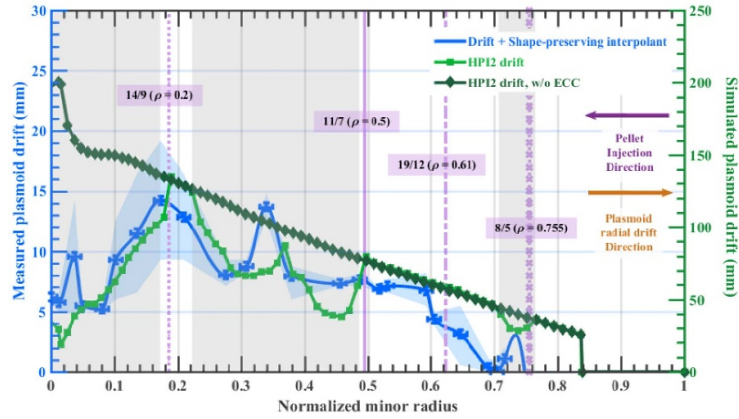
Figure 3. Averaged radial plasmoid drift displacement (blue; a shaded region represents data dispersion) as a function of pellet position for #53344 to #53349. Right axis: HPI2 simulated plasmoid drift (light green squares), compared with the drift when the ECC effect is neglected (dark green diamonds). The strongest low-order rational values are highlighted.

exceeds a critical size and the relative direction of the ∇B associated current are inverted at the two ends of the plasmoid. The circuit is closed by a parallel current inside the plasmoid which reduces its cross-field acceleration [23, 26]. The external circuit closure (ECC) in turn ensues when two oppositely charged regions are connected along the same flux tube, which short-circuits the plasmoid polarization and dampens the drift. ECC is more effective in the vicinity of rational magnetic flux surfaces due to reduced connection lengths [27, 28]. Recently, LHD experiments with impurity-doped pellets have demonstrated that enhanced radiation in the plasmoid is also able to moderate its outward radial drift by reducing its internal pressure [29].

Although ECC is considered of secondary importance in stellarators with respect to ICC [30], a previous study in TJ-II revealed an interaction between plasmoids and low-order rational surfaces attributed to the ECC effect [31]. More recently, this ECC effect has been further studied in TJ-II, both experimentally and theoretically, to evaluate the effect of rational surfaces on particle deposition in stellarators [32]. An illustration of the experimental evidence that ECC has measurable consequences in pellet particle deposition is shown in figure 3. To evaluate plasmoid drift experimentally, the pellet track is monitored with a fast-frame camera with very high temporal resolution and low exposure times, $\leqslant 1\ \mu$s. For a theoretical analysis, the latest stellarator version of the HPI2 code is used [25, 32]. This version has been validated for TJ-II and W7-X [33, 34] and has been used in recent additional studies for these and other helical devices [35, 36]. The HPI2 model shows (and fast camera images confirm) that, for TJ-II conditions, plasmoid lengths along the magnetic field directions, Z_0, are typically in the range $0.1\ \text{m} \leqslant Z_0 \leqslant 0.2\ \text{m}$ a microsecond after the plasmoid detaches from the pellet. Here, Z_0 refers to the parallel extent of the overpressure region where the ablated pellet particles are located (which propagates at sound speed). In this time scale, regions of opposite polarization have already connected to each other by parallel currents (stabilised in an Alfvén transit time). That is, the ECC effect has already started to take place.

Specifically, figure 3 shows the measured radial plasmoid drift displacements for the TJ-II standard magnetic configuration, 100_44_64, ($a = 0.192$ m, $B_0 = 1.08$ T, $\iota_0 = 1.55$, $V_{\text{plasma}} = 1.1$ m^3 where ι_0 is the on-axis rotational transform), averaged for a series of reproducible discharges (from #53344 to #53349). It should be noted that in TJ-II pellets are injected along straight guide tubes with velocities between 800 and 1200 m s^{-1} and they enter the plasma from the outer plasma region, i.e. from the LFS. With this injection geometry, the plasmoid drift is predominantly outwards-directed, that is, opposite to the PI direction. Although a detached plasmoid is sometimes visible, i.e. two independent emission regions are seen, an initial drifting plasmoid is usually observed as an asymmetry of the cloud. From this asymmetry, the initial drift displacement can be estimated. For this, it is assumed that the main contribution to the cloud's luminous intensity is due to the ablation of the pellet, and that there is a secondary contribution attributed to the partially ionised drifting plasmoid. Taking this into account, the light profile recorded by the camera is fitted by two Gaussians, with the difference between the two centres being the drift, as explained in [33]. In this study, only the radial component of the drift is estimated from the asymmetry of the cloud in the radial direction. The experimentally estimated radial drift shown in the figure indicates the radial drift during a 1 μs exposure time for a plasmoid detached at the position given by the horizontal axis. It can be observed that drift displacement tends to increase with pellet penetration depth up to $\rho = \sim 0.6$, where $\rho = r/a$, as drift increases with increasing electron temperature. However, between $\rho = \sim 0.4$ and $\rho = \sim 0.6$, the drift displacement remains mostly constant. This can be attributed to a combination of the effect of rational surfaces and to faster ionisation of the plasmoid due to higher electron temperatures. In addition, some local minima are observed, which can be accounted for by the effect of the rational surfaces (via external closure) in the vicinity of these reductions (such as the 8/5, the 11/7 and/or the 14/9). It should be noted that a deceleration of the drift is to be expected as a plasmoid passes through a rational surface, rather than an immediate braking at exactly the position of the rational

5

surface. The importance of the observed improvement in drift damping should depend on the distance between the origin of the plasmoid and the rational surface. For example, if a plasmoid is created too close to a rational surface, the parallel connection time will be longer than the plasmoid radial drift time-scale and it will drift out before the rational-enhanced ECC effect can act.

The experimental results are compared with HPI2 predictions in figure 3. The simulation input are plasma profiles fitted from Thomson scattering measurements of representative balanced NBI discharges, and an average value of pellet size and velocity from the various injections in the experiments considered. It should be noted that HPI2 provides values of the plasmoid drift at the end of the homogenisation process ($t_{\text{hom}} \sim 500 \ \mu$s), in contrast to the experimental estimations ($t_{\text{exp}} \sim 1 \ \mu$s). This large difference between the two time scales implies that one cannot meaningfully compare the total displacement values. The time scales shown in the plot have been adjusted to allow for an easy comparison of the radial structure of the calculated and measured drift displacements. Although there is a large difference between the two time scales and the experimental measurement cannot give an indication of the total drift displacement (once the degree of ionisation of the plasmoid is high enough it is not possible to observe it with the fast camera), both simulations and experimental data indicate that the maximum drift acceleration is reached very early in the homogenisation phase [33]. Therefore, if the drift displacement is already smaller after 1 μs, because the drift acceleration is already damped, the total drift must necessarily be smaller, since the acceleration becomes negative almost immediately afterwards, i.e. there is no mechanism accelerating the drift after this time. This also implies that general trends and total drift values should not be considered in the analysis. In contrast, only small radial scales are of interest for this comparison. The drift, calculated when the ECC effect is neglected, is also shown in figure 3. For this latter case, the drift is seen to increase continuously with pellet penetration, without any local minima. In contrast, when the ECC effect is considered, the calculated drift is reduced in different regions along the minor radius, which closely resembles the experimental observation. The exception is the region between $\sim0.5 \leqslant \rho \leqslant \sim0.7$, as the total drift with and without the ECC effect is identical. These plasmoids detach from the pellet close enough to the LCFS to reach it during the homogenisation time, even when the ECC effect is damping the drift when they cross the rational surfaces 19/12 and/or 8/5. This cannot be observed experimentally, as the full trajectory of the plasmoids cannot be followed. Besides, plasmoids originating at $\rho > \sim0.75$ fall outside the region of interest considered. Nevertheless, the evaluated drift reductions, within the error bars, occur in general around the same radial positions that were identified from the simulations. For instance, the limited drift for plasmoids detached between $\sim0.0 \leqslant \rho \leqslant \sim0.2$ can be attribute to the interaction with the rational surface 14/9 rational, located at $\rho = 0.2$, i.e. the reduction of the drift is found for plasmoids originated inside the rational surface. Drift reductions for plasmoids born in the radial region

$\sim0.3 \leqslant \rho \leqslant \sim0.5$ are not as clearly observed since the exposure time, 1 μs, is too short for such plasmoids to reach the rational surface 19/12 at $\rho = 0.61$, in addition to the rational surface 11/7. In summary, drift reduction is noticed for plasmoids detached in a given region within a rational surface. In these regions, there is usually a certain distance to the rational surface for which the drift is minimal, as the ECC effect depends both on the distance to the rational surface and on the size of the plasmoid, the connection length and the plasmoid's own drift velocity. Noting these minima drifts may be less obvious when a plasmoid traverses several rational surfaces. Finally, it has been observed that the variation of the magnetic configuration causes a shift of the positions where drift reductions are observed that is consistent with the change in the position of the rational surfaces [32].

From these results it can be first concluded that the ECC effect, normally neglected in stellarators, can play an important role in modifying plasmoid drift in stellarator [32]. Therefore, the choice of the magnetic configuration could enhance core pellet fuelling and particle deposition to achieve a relatively deep and efficient fuelling using LFS pellets in stellarators. The importance of these results is highlighted by the conclusions drawn from the comparison of HPI2 simulations for relevant scenarios in ITER and W7-X [36]. This work underlines the important role of drift damping mechanisms, i.e. ICC and ECC effects, in the final particle deposition.

Some of the activities at TJ-II summarised in this section are part of an on-going multi-device (including W7-X, TJ-II, LHD and Heliotron J) effort to validate the current version of HPI2. While the code reproduces both pellet ablation and particle deposition for the representative cases of TJ-II [33], the results for the other three devices show discrepancies. For example, ablation is very well reproduced in all cases considered so far for all devices (diagnosed by H$_\alpha$ monitors), except for HFS injections in W7-X, possibly due to the strong acceleration of the pellets not taken into account in the simulations [34, 35]. On the contrary, the agreement of the deposition profiles (diagnosed through changes in the density profile) in other stellarator devices is only qualitative and hints at an overestimation of the plasmoid drift. Joint efforts are underway to extend the number of considered cases of the four devices, so that it can be determined whether such discrepancies are due to the simplification of the treatment of the drift in 3D magnetic fields or there are some potential mechanisms missing in the HPI2 homogenisation model.

4. Profile shaping—enhanced plasma performance after PI

As noted previously, PI is used in magnetic confinement fusion devices to achieve deep and efficient core plasma fuelling. Moreover, improved post-injection plasma performance has been reported for many devices, both tokamaks and stellarators, after PI [37, 38]. Recently, when a train of slow pellets is injected into ECRH plasma in the stellarator W7-X, a transient increase in energy confinement time is observed, this

resembling several aspects of enhanced confinement after gas-puff or PI in other fusion devices [39, 40]. In neutral beam injection heated plasmas of TJ-II, an enhanced performance phase can be induced, and maintained until discharge completion, after a single hydrogen pellet (1×10^{19} to 2.2×10^{19} H atoms) is injected when the target line-averaged electron density, $<n_e>$, is $\sim$1.5 to $\sim$2 $\times 10^{19}$ m^{-3} [41]. In such cases, the pellet is injected from the outer plasma edge and due to a low electron temperature, $T_e \leqslant 400$ eV, ice penetrates beyond the magnetic axis. Since detached pellet clouds generally drift radially outwards, the injection causes the central density to increase significantly inside $\rho = 0.7$ with little or no change outside this radius.

A clear characteristic of this new scenario is a strong increase in the stored diamagnetic energy, W^E_{diag}, as determined with a diamagnetic loop, as well as in the energy confinement time, τ^E_{diag}, i.e. by up to 40% when compared to predictions obtained using the International Stellarator Scaling law, τ^E_{ISS04}, rescaled for TJ-II [42]. Moreover, the plasma triple product, $n_e \cdot T_i \cdot \tau^E$, is seen to exhibit a clear bifurcation point after PI towards an improved confinement branch when compared to ISS04 scaling-law predictions (a bifurcation is understood to be a significant improvement in plasma confinement properties for unchanged external drive system values (NBI heating) that lasts significantly longer than the initial transitory pellet-induced density enhancement) [41]. The Pellet-induced Enhanced Confinement (PiEC) phase is characterized by more intense radial density gradients in the region about $\rho = 0.6$. Additionally, a more negative radial electric field, E_r, across a broad plasma region and a reduction in density and plasma potential fluctuations close to $\rho = 0.5$ are measured using a Heavy Ion Beam Probe. These are accompanied by a higher central beta and volume-averaged beta, i.e. by up to 70% and to $\sim$35%, respectively when compared to a reference discharge made under the same conditions. In order to help understand this improved performance phase, neoclassical calculations were performed for such plasmas with/without PI [41]. While not allowing identification of a mechanism for such improved performance, neoclassical calculations predicted more negative E_r and increased τ^E_{diag} which qualitatively agree with experimental tendencies. However, the contribution of turbulence reduction to these improvements in performance still needs to be quantified.

The characterisation of the PiEC at TJ-II, which is, in many respects, analogous to the post-pellet regimes found at W7-X has been the objective of recent experimental efforts [39, 40, 43]. In particular, studies on the optimization and sustainment of the confinement enhancement are briefly described next. We refer the reader to [44] for further details.

Different sized pellets (with 5×10^{18} to 2.2×10^{19} H atoms) were injected in sequence with time separations $\geqslant$5 ms into NBI-heated plasmas to further investigate this PiEC phase in TJ-II. In a first instance, experiments were performed by injection a large initial pellet followed by 1 or 2 smaller pellets (a total of $\leqslant$3.5 $\times 10^{19}$ H atoms). A strongly peaked density profile is achieved after the initial pellet ($\sim$2.2 $\times 10^{19}$

H atoms) and this profile is broadened as the additional pellets were injected ($\leqslant$1.2 $\times 10^{19}$ H atoms per pellet). In contrast, the injection of the pellets resulted in only a slight reduction in core T_e. As a result of these injections, the post-injection line-averaged electron density was kept below $\sim$5 $\times 10^{19}$ m^{-3} and the NBI-maintained plateau phase terminated only after switch-off. In addition, post-injection τ^E_{diag} values were longer than values reported for single PIs, by up to 20% in some cases. Moreover, significant improvement was achieved with respect to ISS04 scaling-law predictions (see figure 12 of [44]). To date, such pellet-induced improved performance phases have been achieved and maintained using a single NBI counter-injector (with 450 kW of port-through power injected roughly parallel to the magnetic field) along a plateau phase and stored maximum diamagnetic energies up to 4.7 kJ have been achieved. In experiments without pellets, the highest W^E_{diag} achieved with the same NBI system and port-through power is of the order 3 kJ for $<n_e> = \sim$5 $\times 10^{19}$ m^{-3}.

In another PI experiment [44], two of the largest available pellets (containing up to 6×10^{19} H atoms) were injected into plasma heated by 450 kW of counter-injected NBI power. See figures 6 and 7 in [44]. In the discharge the stored diamagnetic energy increases steadily after the 1st PI and continues to do so at a steady rate until it reaches $\sim$4.7 kJ when the line-averaged density approaches $\sim$6 $\times 10^{19}$ m^{-3}. However, the improved performance plateau phase is not sustained, rather the plasma decays slowly as $<n_e>$ rises above 6×10^{19} m^{-3}, suggesting a thermal quench rather than a radiation collapse as post-injection Z_{eff} reduces from about 1.4–1.1 (boron and lithium coatings are performed on the vacuum chamber walls to keep this factor low in TJ-II). In comparison, a maximum stored diamagnetic energy close to 3 kJ is achieved for a reference discharge without PI with the same heating and wall conditions, i.e. #55511. See figures 6 and 7 of [44]. This latter W^E_{diag} value is representative of maximum values reported to date for similar TJ-II experimental conditions when using counter NBI heating and similar wall conditions. In the same figure, the W^E_{dia} plateau of #55511 begins to decay before NBI switch-off, this decay beginning at 1215 ms when $<n_e> = \sim$5.3 $\times 10^{19}$ m^{-3}. If this value is representative for counter NBI heated plasmas, then PIs result in $\sim$15% increase in maximum sustainable density in TJ-II.

In parallel to the optimization and sustainment of the PiEC phase, its main dependencies (isotope mass, magnetic configuration and field direction) are being investigated at TJ-II. Here we report on latter: TJ-II is operated normally with its magnetic field orientated in the anti-clockwise direction when viewed from above the device. See, for instance, figure 1 of [31]. This orientation is preferred as the dual heavy ion beam probe diagnostic system is designed for this field direction. Now, in another set of experiments, PIs were performed when TJ-II was operated with its *B* field direction reversed, i.e. following a clockwise direction when viewed from above, and for plasmas heated with a single NBI injecting parallel to the reversed magnetic field (i.e. in co-injection). PIs were made with this set-up in order to determine if a PiEC phase
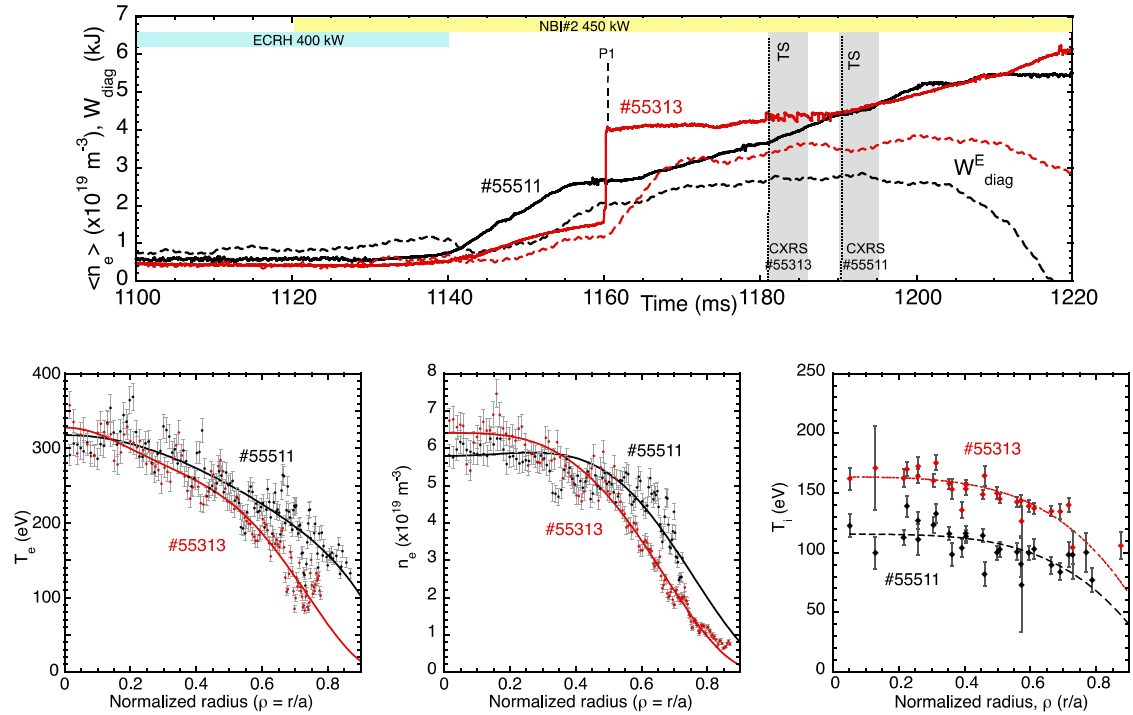
Figure 4. Top: Temporal evolution of line-averaged electron density (continuous) and stored diamagnetic energy (dash–dash) along 2 TJ-II discharges (#55511 (black) without PI and #55313 (red) with PIs at 1160 ms and 1166 ms). TS and CXRS measurements are made when $\langle n_e \rangle = 4.5 \times 10^{19}$ m^{-3} for both discharges. Bottom lhs and centre: TS profiles for T_e and n_e obtained at 1182 ms for #55313 and at 1191 ms for #55511. Bottom rhs: Ti profiles measured by charge exchange recombination spectroscopy from 1182 to 1187 ms for #55313 (red) and from 1190 ms to 1195 ms for #55511 (black). Error bars indicate uncertainties in the spectral fitting.

with similar enhanced parameters could be achieved in TJ-II with co-NBI heating and to confirm if post-injection density profiles are independent of B field direction. The latter is expected as the radial direction of plasmoid drift acceleration, $\delta V_d / \delta t = 2(P_0 - P_\infty)/(L_B\, N_0\, m_i)$, should be independent of B-field direction, i.e. similar post-injections density profiles would be expected [25], where P_0 and P_∞ are plasmoid and plasma pressures, $L_B = B_\infty / \nabla_\perp B_\infty$, the magnetic cross-field gradient scale-length, is close to 1 m^{-1} in TJ-II, N_0 is plasmoid density and m_i is ion mass. When PI experiments are repeated using a similar set-up but with B reversed, it is found that pellet induced increases in W^E_{diag} and τ^E_{diag} are similar for both field directions and similar post-injection T_e, n_e and T_i profiles are achieved. Such results indicate that PiEC development and maintenance is independent of B-field toroidal direction and of co-counter or counter NBI heating in the TJ-II.

Recently, a diagnostic NBI-based spectroscopic system was recommissioned on TJ-II for performing Charge-Exchange Recombination Spectroscopy (CXRS) on the C VI emission line at 529 nm to obtain a single T_i profile per discharge [45]. This has allowed to quantify a substantial improvement in the ion energy content during the PiEC phase. In figure 4, we compare a discharge (#55313) with a single PI (2.3×10^{19} H atoms) to a reference plasma without PI (#55511) but with similar line-average electron densities when TS and CXRS measurements are made. Both plasmas are heated by 450 kW of co-counter NBI power and the same

standard magnetic configuration is employed. In these discharges, where $W^E_{\text{diag}} = 3.4$ kJ for #55313 and $W^E_{\text{diag}} = 2.9$ kJ for #55313 when TS and CXRS measurements are made, central T_e are n_e are similar to within $\pm 10\%$ whilst the electron kinetic profiles for #55313 (1 PI) are narrower than those for #55511 (no PI). However, in the case of the T_i profiles, it is seen that the PI has caused the central T_i to increase by $\sim 45\%$ and its profile to broadened considerably. During the short time period when a pellet is ablated and when pellet particles homogenize with background plasma ($< \sim 1$ ms), total plasma energy should be conserved if ionization and radiation losses are negligible [46]. In order to interpret the increase of ion temperature, it is necessary to recall that, for NBI-heated discharges in TJ-II, electron heating dominates, ($E_{\text{beam}} = 30$ keV and the full, half and third energy beam content is 55%, 20% and 25%, respectively), with about 75% of the 30 keV fast ion energy being deposited in the electrons. This ratio depends primarily on the electron temperature, whereas the neutral beam ion slowing-down time depends on T_e and n_e. The direct ion NB-heating is therefore expected to be very similar in the two cases. The largest contribution to ion heating in TJ-II is electron–ion energy transfer, which is proportional to the electron–ion temperature difference and the collisional transfer coefficient $\sim n_e^2\, T_e^{-3/2}$. Referring again to the profiles in figure 4, we conclude that the reduction of the e–i temperature difference should result in a lower ion heating, hence a lower ion radial heat flux, in the PiEC phase. This, together with a larger ion energy content, results in an improved ion energy
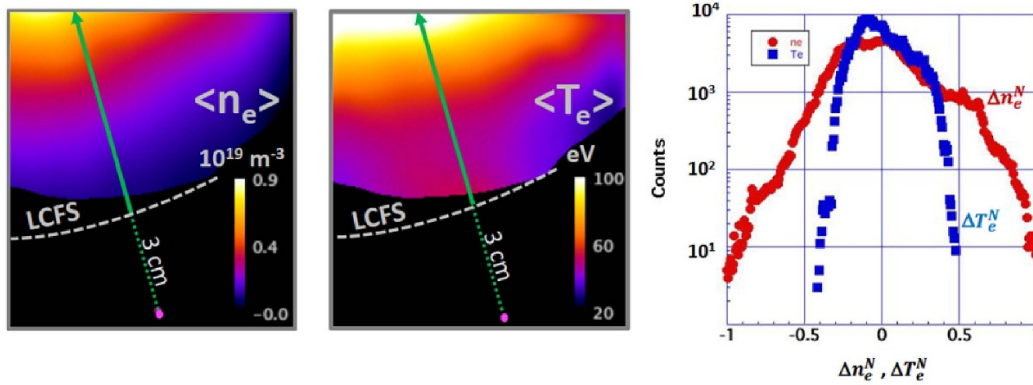
Figure 5. Left 2D colour plots: electron density and temperature maps of an ECRH plasma averaged over 2 ms. The approximate position of the last closed flux surface and a radial chord (green arrow) are indicated. Right: relative probability distribution functions of n_e and T_e fluctuations normalized to their time-averaged values (all pixels included).

confinement. Local power balance analysis and gyrokinetic modelling of the two conditions will be the subject of future studies to quantify and understand the reduction of the ion heat diffusivity.

Finally, a simplified turbulence model based on resistive MHD equations, that is known to model turbulent dynamics of the TJ-II successfully, at least in a qualitative sense, has been used in an attempt to identify possible dynamical mechanics that can account for the observed post-injection improved confinement and modified density gradients [47]. In this reference, it is noted how, for instance, an increase in the density gradient created by a pellet excites resistive interchange modes at low-order rational surfaces. It is described in [47] how instabilities show strong mutual coupling and create multiple transport barriers through associated zonal flows. This strongly nonlinear dynamic process could be responsible for the confinement improvement. Although experimental and model confinement times cannot be compared directly, since energy confinement time is measured and particle confinement time is calculated, qualitative agreement is obtained in terms of improved confinement. We note that the change in the density profile that follows the pellet deposition process has been shown to be consistent with neoclassical transport [48]. Gyrokinetic simulations in a flux tube geometry with kinetic electrons show a stabilizing effect of the density gradient on the gyrokinetic turbulent heat flux [49], which seems qualitatively consistent with W7-X and TJ-II observations. A quantitative comparison between the simulated gyrokinetic flux and that resulting from the experimental power balance analysis is left for a future work.

5. Advanced edge diagnosis-two-dimensional fluctuation measurements and neutral-turbulence interaction

In fusion research, there are numerous observations of the importance of the fuelling rate (via either recycling or puffing) for determining overall plasma performance. At TJ-II and other devices, wall coating with lithium has been shown to

improve plasma confinement [6] and the proposed explanations point to the reduced recycling and edge neutral population having a positive effect on turbulent plasma transport [50]. The interaction of neutrals with turbulence has been studied experimentally for the first time using the fast 2D-imaging of three neutral helium lines at TJ-II, providing evidence for the reaction of helium neutrals on turbulent time-scales [51]. This is explained in that reference in the following way: the local n_e variations of positive blobs (filaments) produce due to ionization reactions the depletion of the neutrals there. In this way, the neutrals follow inversely the n_e fluctuations. This coupling of plasma turbulence to neutrals is also being studied using kinetic codes and simulations [7, 52–55]. Last year, an upgraded spectroscopic camera system has been commissioned in TJ-II that allows simultaneous 2D-measurement of the edge n_e and T_e with exposure times down to 5 μs, frame rates of up to 90 kHz and spatial resolution better than 5 mm [56]. The well-established He I-Ratio technique is applied to the 3 emission images recorded by the system viewing the neutral He cloud injected into the plasma. The line of view is nearly parallel to the magnetic field in order to optimize the spatial resolution when observing field-aligned coherent structures (filaments). A software framework has been developed to semi-automatically extract the n_e and T_e images from the camera data. It aligns the images, applies calibration factors and finally calculates the 2D n_e and T_e fields using a database containing estimates from a Collisional-Radiative-Model. Error propagation in this processing is being developed.

The two colour plots in figure 5 show the 2D maps of electron density and temperature averaged over 2 ms for an ECRH plasma. Regions where the signal level is insufficient are coloured in black. The green arrows indicate the approximate radial direction. Preliminary studies for ECRH plasmas show that the amplitude of the normalized (relative) fluctuations are 2–3 times higher for n_e than for T_e, as can be seen from the probability distribution functions plotted in figure 5 right. We have also seen that the turbulence level increases with injected ECRH power in both channels, n_e and T_e. The analysis of last campaign's results is in progress, including the study of the n_e–T_e 2D-field cross-correlation together with error propagation

analysis. Once this is done, we will proceed with the quest of the plasma turbulence—neutral coupling as explained in [51]. Finally, in parallel to the analysis effort, the experimental set-up is being upgraded with the acquisition of a new GEN III image intensifier (Hamamatsu C16031) and a faster camera (Photron Nova S-20) to improve the signal to noise ratio and to increase the recording speed. Results are in preparation and will be presented soon.

6. Summary

State-of-the-art experimental techniques, models and codes are at use at TJ-II to improve our understanding of particle fuelling and transport in view of the importance of developing predictive capabilities for density profiles in next-step stellarator devices. Gyrokinetic simulations with realistic gradients have shown that inward turbulent convection may be behind the shape of core density profiles observed in stellarators. PIs at TJ-II together with fast camera measurements are helping elucidate the importance of rational surfaces in plasmoid dynamics. Furthermore, TJ-II successfully demonstrates a large performance enhancement following PI in NBI plasmas. Such an enhancement significantly outlasts both the particle and energy confinement times, indicating a bifurcation of the plasma state. The quantification of heat diffusivity reduction in this regime and its gyrokinetic modelling will be the subject of future studies at TJ-II. Finally, plasma edge 2D observation techniques are being refined at TJ-II to investigate fluctuations in the electron density and temperature and the interaction of neutrals with plasma turbulence.

ORCID iDs

J.A. Alonso https://orcid.org/0000-0001-6863-8578
A. Baciero https://orcid.org/0000-0003-1717-3509
M. Barnes https://orcid.org/0000-0002-0177-1689
E. de la Cal https://orcid.org/0000-0001-8020-7682
I. Calvo https://orcid.org/0000-0003-3118-3463
A. Cappa https://orcid.org/0000-0002-2250-9209
D. Carralero https://orcid.org/0000-0002-7824-3307

References

[1] Weller A. *et al* 1991 *Plasma Phys. Control. Fusion* **33** 1559
[2] Sudo S., Takeiri Y., Zushi H., Sano F., Itoh K., Kondo K. and Iiyoshi A. 1990 *Nucl. Fusion* **30** 11
[3] Thienpondt H. *et al* 2023 *Phys. Rev. Res.* **5** L022053
[4] Dinklage A. *et al* Controlling performance bifurcations in large stellarators *2023 IAEA Fusion Energy Conf.* (*London, 16–21 October 2023*) p 1820 (available at: https://www.iaea.org/events/fec2023)
[5] Alonso J.A., Calvo I., Carralero D., Velasco J.L., García-Regaña J.M., Palermo I. and Rapisarda D. 2022 *Nucl. Fusion* **62** 036024
[6] Tabarés F.L. *et al* 2008 *Plasma Phys. Control. Fusion* **50** 124051
[7] Tamain P. *et al* 2023 European edge fluid modelling tools for self-consistent reactor relevant conditions *2023 IAEA Fusion Energy Conf.* (*London 16–21 October*) p 2319 (available at: https://www.iaea.org/events/fec2023)
[8] Ricci P. *et al* 2023 Theoretical scaling of the operational density limit in tokamaks and comparison to experimental data *2023 IAEA Fusion Energy Conf.* (*London 16–21 October*) p 1994 (available at: https://www.iaea.org/events/fec2023)
[9] Ochando M. *et al* 2014 *41st EPS Conf. on Plasma Physics* (*Berlin*, *23–27 June)* (available at: https://lac913.epfl.ch/epsppd3/2014/pdf/P2.074.pdf)
[10] Fernández-Ruiz D., Losada U., Ochando M.A., Liu B. and Hidalgo C. (the TJ-II Team) 2021 *Nucl. Fusion* **61** 126038
[11] Itoh K. and Itoh S.-I. 1988 *J. Phys. Soc. Japan* **57** 1269
[12] Zanca P., Sattin F., Escande D.F., Pucella G. and Tudisco O. 2017 *Nucl. Fusion* **57** 056010
[13] Fuchert G. *et al* (W7-X Team) 2020 *Nucl. Fusion* **60** 036020
[14] Bañón Navarro A., Di Siena A., Velasco J.L., Wilms F., Merlo G., Windisch T., LoDestro L.L., Parker J.B. and Jenko F. 2023 *Nucl. Fusion* **63** 054003
[15] Maassberg H., Beidler C.D. and Simmet E.E. 1999 *Plasma Phys. Control. Fusion* **41** 11350
[16] Beidler C.D., Feng Y., Geiger J., Köchl F., Maßberg H., Marushchenko N.B., Nührenberg C., Smith H.M. and Turkin Y. 2018 *Plasma Phys. Control. Fusion* **60** 105008
[17] Tanaka K. 2010 *Fusion Sci. Technol.* **58** 70–90
[18] Tallents S. *et al* 2014 *Plasma Phys. Control. Fusion* **56** 075024
[19] Sánchez E., Estrada T., Velasco J.L., Calvo I., Cappa A., Alonso A., García-Regaña J.M., Kleiber R. and Riemann J. (the TJ-II Team) 2019 *Nucl. Fusion* **59** 076029
[20] Angioni C., Fable E., Greenwald M., Maslov M., Peeters A.G., Takenaga H. and Weisen H. 2009 *Plasma Phys. Control. Fusion* **51** 124017
[21] Sharma R. *et al* 2020 *Phys. Plasmas* **27** 062502
[22] Van Milligen B., Carreras B.A., Voldiner I., Losada U. and Hidalgo C. 2021 *Phys. Plasmas* **28** 092302
[23] Rozhansky V.A., Senichenkov I., Veselova I. and Schneider R. 2004 *Plasma Phys. Control. Fusion* **46** 575–91
[24] Parks P.B. and Baylor L.R. 2005 *Phys. Rev. Lett.* **94** 1–4
[25] Pegourie B., Waller V., Nehme H., Garzotti L. and Géraud A. 2007 *Nucl. Fusion* **47** 44–56
[26] Senichenkov I.Y., Veselova I.Y., Rozhansky V.A. and Schneider R. 2005 *J. Nucl. Mater.* **337–339** 446–50
[27] Commaux N., Pégourié B., Baylor L.R., Köchl F., Parks P.B., Jernigan T.C., Géraud A. and Nehme H. 2010 *Nucl. Fusion* **50** 025011
[28] Sakamoto R., Pégourié B., Clairet F., Géraud A., Gil C., Hacquin S. and Köchl F. 2013 *Nucl. Fusion* **53** 063007
[29] Matsuyama A., Sakamoto R., Yasuhara R., Funaba H., Uehara H., Yamada I., Kawate T. and Goto M. 2022 *Phys. Rev. Lett.* **129** 255001
[30] Matsuyama A., Koechl F., Pégourié B., Sakamoto R., Motojima G. and Yamada H. 2012 *Nucl. Fusion* **52** 123017
[31] McCarthy K.J. *et al* (TJ-II Team) 2021 *Nucl. Fusion* **61** 076014
[32] Panadero N., McCarthy K.J., Pégourié B., Carrasco R., García-Cortés I., García R., Hernández-Sánchez J., Köchl F., Martínez-Fernández J. and Sakamoto R. 2023 *J. Plasma Phys.* **89** 955890601
[33] Panadero N. *et al* (TJ-II Team and W7-X Team) 2018 *Nucl. Fusion* **58** 026025
[34] Baldzuhn J. *et al* 2019 *Plasma Phys. Control. Fusion* **61** 095012
[35] Panadero N. *et al* 2022 *48th European Physical Society Conf. Plasma Physics, EPS* (*Online*, *27 June–1 July*)
[36] Panadero N. *et al* 2023 *Nucl. Fusion* **63** 046022
[37] Sakamoto R. *et al* 2001 *Nucl. Fusion* **41** 381
[38] Lang P.T. *et al* (ASDEX Upgrade Team) 2018 *Nucl. Fusion* **58** 036001

[39] Baldzuhn J. *et al* 2020 *Plasma Phys. Control. Fusion* **62** 055012

[40] Bozhenkov S. *et al* (W7-X Team) 2020 *Nucl. Fusion* **60** 066011

[41] García-Cortés I. *et al* 2023 *Phys. Plasmas* **30** 072506

[42] Yamada H. *et al* 2005 *Nucl. Fusion* **45** 1684

[43] Estrada T. *et al* (W7-X Team) 2021 *Nucl. Fusion* **61** 046008

[44] McCarthy K.J. *et al* (TJ-II Team) 2024 *Nucl. Fusion* **64** 066019

[45] Carmona J.M., McCarthy K.J., Balbín R. and Petrov S. 2006 *Rev. Sci. Instrum.* **77** 10F107

[46] McCarthy K.J. *et al* (the TJ-II Team) 2017 *Nucl. Fusion* **57** 056039

[47] García L., García-Cortés I., Carreras B.A., McCarthy K.J. and van Milligen B.P. 2023 *Phys. Plasmas* **30** 092303

[48] Velasco J.L. *et al* 2016 *Plasma Phys. Control. Fusion* **58** 084004

[49] Thienpondt H., García-Regaña J. M., Calvo I., Acton G. and Barnes M. Influence of the density gradient on turbulent heat transport at ion-scales: an inter-machine study with the gyrokinetic code stella (arXiv:2404.09929)

[50] Krasheninnikov S.I., Zakharov L.E. and Pereverzev G.V. 2003 *Phys. Plasmas* **10** 1678–82

[51] de la Cal E. (The TJ-II Team) 2016 *Nucl. Fusion* **56** 106031

[52] Wersal C. and Ricci P. 2015 *Nucl. Fusion* **55** 123014

[53] Thrysoe A.S., Løiten M., Madsen J., Naulin V., Nielsen A.H. and Rasmussen J.J. 2018 *Phys. Plasmas* **25** 032307

[54] Stotler D.P., Ku S., Zweben S.J., Chang C.S., Churchill R.M. and Terry J.L. 2019 *Nucl. Mater. Energy* **19** 113

[55] Coroado A. and Ricci P. 2022 *Nucl. Fusion* **62** 036015

[56] Voldiner I. *et al* 2022 *48th European Physical Society Conf. Plasma Physics, EPS* (*Online, 27 June–1 July)* (available at: https://info.fusion.ciemat.es/OCS/EPS2022PAP/pdf/P2b.106.pdf)